THE ASTROPHYSICAL JOURNAL, 1008:127 (9pp), 2026 September 1 https://doi.org/10.3847/1538-4357/ae9150

Asymmetric Distribution of Electron Density near Enceladus: A Comparative Survey of Upstream and Downstream Cassini Flybys

Fiona Wai Chung Law[1,2], Dingnuo Wang[1,3], Yin Ching Law[4], Zhonghua Yao[1,2,5], Shangchun Teng[1], and Binzheng Zhang[1,2]
[1] Department of Earth and Planetary Sciences, The University of Hong Kong, Hong Kong, People's Republic of China
[2] The Hong Kong Institute for Astronomy and Astrophysics, The University of Hong Kong, Hong Kong, People's Republic of China
[3] Hefei 168 High School, Hefei, Anhui Province, People's Republic of China
[4] School of Computing and Data Science, The University of Hong Kong, Hong Kong, People's Republic of China
[5] Laboratory for Space Research, Faculty of Science, The University of Hong Kong, Hong Kong, People's Republic of China
Received 2026 May 18; revised 2026 July 23; accepted 2026 July 27; published 2026 August 31

Abstract

Enceladus is a key source of plasma and neutrals in Saturn's magnetosphere through its active south polar plume, which drives complex dust–plasma interactions and modifies the local environment. In this paper, we investigate electron density perturbations near Saturn's moon Enceladus using Cassini observations from 12 targeted flybys that sampled the upstream and downstream regions. Electron densities are derived from the upper hybrid resonance frequencies detected by the Radio and Plasma Wave Science (RPWS) instrument, and energetic electron intensities are obtained from the Low Energy Magnetospheric Measurement System (LEMMS) of the Magnetospheric Imaging Instrument. Flybys are classified as upstream or downstream encounters, enabling a direct comparison of spatial variations. The results reveal a pronounced upstream–downstream asymmetry in RPWS electron density. Downstream flybys exhibit strong depletions near Enceladus, with anomalies reaching up to ∼60 cm^{-3} below background levels, whereas upstream flybys display only modest variations of a few cm^{-3}. The magnitude of dropouts in the downstream region also depends on flyby geometry. These observations are consistent with the presence of plume-generated dust and Alfvén wings downstream and offer insight into the spatial scale of the interaction region. In contrast, LEMMS energetic electron observations show no clear upstream–downstream asymmetry, with intensity dropouts occurring in both geometries. This may indicate that cold and energetic electron populations exhibit different behaviors influenced by physical processes operating on different spatial scales in the vicinity of Enceladus.

Unified Astronomy Thesaurus concepts: Enceladus (2280); Saturn (1426); Saturnian satellites (1427)

1. Introduction

Saturn's space environment is a dynamic and complex system shaped by its strong magnetic field, material influx from both the solar wind and internal sources such as Enceladus' water plume, planetary rotation, and solar-wind-driven perturbations. The interplay of these components drives a variety of complex dynamical processes, generating energetic particles and stunning aurora at the poles of Saturn.

Enceladus, Saturn's sixth-largest moon, plays a particularly important role in influencing Saturn's space environment through its complex interactions with Saturn's corotating magnetospheric plasma. The discovery of an active water vapor plume emanating from the tiger stripes near its south pole (M. K. Dougherty et al. 2006; C. J. Hansen et al. 2006; C. C. Porco et al. 2006; F. Spahn et al. 2006; J. H. Waite et al. 2006) revealed Enceladus to be a major source of material for Saturn's E ring (C. C. Porco et al. 2006) and a significant contributor to the neutral and plasma populations in Saturn's magnetosphere (D. H. Pontius Jr. & T. W. Hill 2006; H. T. Smith et al. 2010). Furthermore, neutral gas emitted by the plume is ionized primarily through charge exchange with the ambient magnetospheric plasma, and to a smaller extent by photoionization and electron impact ionization, producing pickup ions that are subsequently incorporated into the corotational flow (R. L. Tokar et al. 2006). This process results in magnetic field perturbations and the formation of Alfvén wings that connect the moon to Saturn's ionosphere (M. K. Dougherty et al. 2006; S. Simon et al. 2011).

The Cassini mission, which orbited Saturn from 2004 to 2017, provided an unprecedented opportunity to study the interaction between Saturn's space environment and Enceladus. Throughout the 13 yr mission, it carried out 23 Enceladus-targeted flybys. Its comprehensive instrument set enabled detailed measurements of magnetic field, plasma populations, energetic particles, and neutral species in the vicinity of the moon. In particular, previous studies have reported perturbations in electron density as Cassini performed close flybys of Enceladus. W. M. Farrell et al. (2009) reported a substantial electron density depletion during the E3 encounter based on upper hybrid emission detected by Cassini's Radio and Plasma Wave Science (RWPS) instrument and attributed it to the absorption of electrons by submillimeter water-ice dust grains. Data from the Langmuir probe of RPWS also show a systematic decrease in electron density as the spacecraft traversed the downstream region of Enceladus owing to dust attachment, while significant enhancements were observed when Cassini passed through the plume (M. W. Morooka et al. 2011; I. A. D. Engelhardt et al. 2015). Consistent with these findings, electron densities inferred from plasma oscillations due to dust impact as detected by RPWS exhibit similar patterns (S. Y. Ye et al. 2014). In the high-energy channel, the Cassini Magnetospheric Imaging Instrument (MIMI) Low Energy Magnetospheric Measurement System

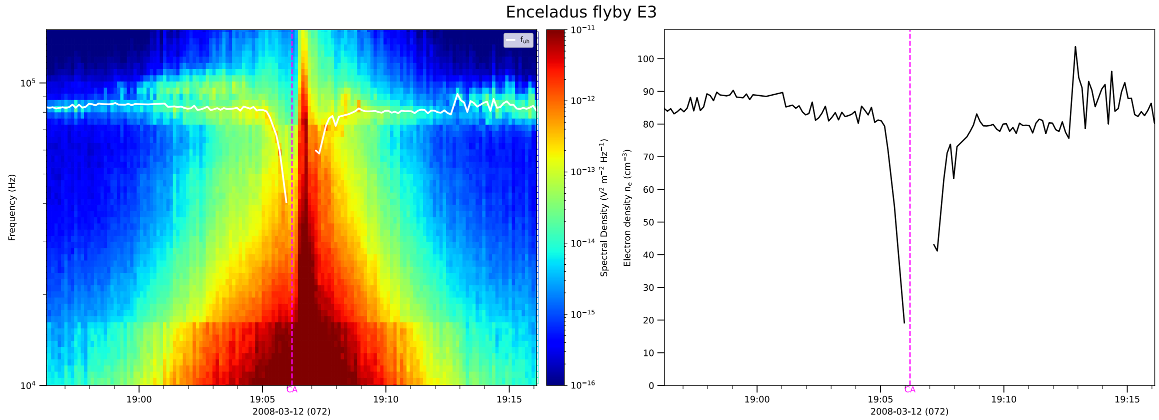

Figure 1. Cassini RPWS data for the E3 flyby on 2008 March 12. The left panel shows the low-rate electric field spectrogram, overplotted with a white line tracing $f_{\rm uh}$ as provided in the dataset. The right panel shows the corresponding derived electron density. The time of closest approach is marked by the magenta dashed line in both panels. Electron density data are absent for a short interval near closest approach due to obscuration of the upper hybrid emission line in the spectrogram by dust impact signals.

(LEMMS) detected characteristic dropouts in energetic electron intensities. These signatures could be classified into full absorptions, ramp-like features, and short dropouts, and have been interpreted as losses of bouncing and drifting electrons onto the moon or plume material (N. Krupp et al. 2012; N. Krupp et al. 2018). These past studies, which examined data of individual or multiple flybys from various instruments, have provided important insights into the spatial distribution of electrons and associated physical processes in the vicinity of the moon.

Despite the advances, comprehensive comparisons of electron density variations between upstream and downstream flybys remain limited. Moreover, combined analyses spanning both low- and high-energy electron populations are still lacking. Such studies would be helpful for further characterizing the spatial structure of electron perturbations and improving our understanding of physical processes near the moon.

In this study, we present a comprehensive analysis of electron density variations as a function of Cassini flyby geometry (upstream versus downstream), using electron densities derived from the RPWS upper hybrid resonance frequency ($f_{\rm uh}$). We also compare these results with LEMMS observations to investigate differences in variation patterns between cold and hot electron populations. In Section 2, we briefly describe the instruments and data used in this study. Section 3 presents the data analysis results. Lastly, Section 4 discusses our physical interpretations and summarizes the key findings.

2. Data and Methods

2.1. RPWS Electron Density

The electric field detector of Cassini's RPWS provides electric field spectrograms, from which the upper hybrid emission line is identified and $f_{\rm uh}$ is derived (D. A. Gurnett et al. 2004). Electron density $n_{\rm e}$ (in $\rm cm^{-3}$) is then obtained from $f_{\rm uh}$ (in Hz) and electron cyclotron frequency $f_{\rm ce}$ (in Hz) based on the equation

$$n_e = \frac{f_{\rm uh}^2 - f_{\rm ce}^2}{8980^2} \qquad (1)$$

(D. A. Gurnett & A. Bhattacharjee 2005). In this study, we use RPWS electron density data from NASA's Planetary Data System (A. M. Persoon et al. 2019). Note that electron density data for certain flybys (e.g., E3, E4, E5, and E6) are unavailable near closest approach for a short time because the upper hybrid emission line is obscured by broadband signals generated by micrometer-sized dust impacts (W. S. Kurth et al. 2006; Z. Wang et al. 2006; W. M. Farrell et al. 2009). The two panels in Figure 1 show an example of the RPWS spectrogram and the corresponding derived electron density during the E3 flyby on 2008 March 12.

To facilitate comparison among multiple flybys, we define the electron density anomaly Δn_e as

$$\Delta n_e = n_e(t) - n_{e,\rm bg}, \qquad (2)$$

where $n_e(t)$ is the electron density at time t and $n_{e,\rm bg}$ is the background electron density for a specific flyby. The background density is defined as the mean density measured outside the immediate interaction region, where the electron density remains relatively stable, typically at radial distances greater than 8–12 $R_{\rm Enc}$ from Enceladus. The exact ranges of radial distances used to determine $n_{e,\rm bg}$ for individual flybys are selected based on data availability and quality. This background subtraction removes large-scale temporal variations of the ambient magnetospheric electron density (A. M. Persoon et al. 2020) and isolates the local perturbations associated with interaction processes.

2.2. MIMI/LEMMS Electron Intensity

LEMMS is one of the three sensors of MIMI, which measures energetic electron and ion fluxes over a broad energy range (S. M. Krimigis et al. 2004). In this study, we use data from LEMMS electron channel E4, which covers the energy range 790–4750 keV. This channel is chosen because it can represent the high-energy electron population and has no known contaminations, for example by electrons of other energy ranges (N. Krupp et al. 2020), protons (C. Paranicas et al. 2022), or UV light (N. Krupp et al. 2018). The energetic electron intensity is measured in units of $\rm cm^{-2}\,sr^{-1}\,s^{-1}\,keV^{-1}$. Note that in contrast to the RPWS data, which provide local

Table 1
Summary of Cassini Enceladus Flybys Used in This Study

Flyby	Date	Closest Approach Altitude (km)	Geometry
E0	2005 Feb 17	1264	Upstream, horizontal
E1	2005 Mar 19	498	Upstream, horizontal
E2	2005 Jul 14	167	Upstream, inclined
E3	2008 Mar 12	48	Downstream, inclined
E4	2008 Aug 11	50	Downstream, inclined
E5	2008 Oct 9	26	Downstream, inclined
E6	2008 Oct 31	170	Downstream, inclined
E8	2009 Nov 21	1597	Downstream, horizontal, far south
E10	2010 May 18	437	Upstream, horizontal
E15	2011 Oct 19	1230	Downstream (far), horizontal
E16	2011 Nov 6	497	Upstream, horizontal
E20	2015 Oct 14	1844	Downstream, horizontal, far north

omnidirectional electron densities, the LEMMS electron intensities from channel E4 are directional, with measurements taken at one specific pitch angle at a given time (J. Vandergriff et al. 2018; J. Vandegriff 2024).

For each flyby, we define an electron intensity ratio R_I as

$$R_I = \frac{I_{\min}}{I_{\mathrm{bg}}}, \tag{3}$$

where $I_{\min}$ is the minimum electron intensity observed and I_{bg} is the background electron intensity estimated beyond the immediate interaction region where the intensity remains relatively stable. A ratio instead of difference is used here to accommodate intensity variations across orders of magnitude with flybys.

2.3. Flyby Selection and Classification

An Enceladus-centered Cartesian coordinate system is adopted in this study. The x-axis points in the direction of the corotating magnetospheric plasma flow, the y-axis points toward Saturn, and the z-axis is aligned with Saturn's rotation axis (approximately northward). Negative x corresponds to the upstream region, while positive x marks the downstream region. Distances are expressed in units of Enceladus radii ($R_{\mathrm{Enc}} = 252.1$ km).

Between 2005 and 2015, Cassini performed 23 flybys targeting Enceladus. For this study, we select 12 flybys and classify them as ideal upstream or downstream events based on spacecraft trajectory. Table 1 summarizes the key parameters and Figure 2 visualizes the trajectories for all flybys used in this study. Five flybys (E0, E1, E2, E10, and E16) are categorized as upstream encounters, sampling the upstream region when Cassini approached Enceladus. The remaining seven flybys (E3, E4, E5, E6, E8, E15, and E20) are categorized as downstream encounters, which traversed the downstream geometric wake of Enceladus or passed above or below it. As the goal of this study is to compare electron density patterns in the upstream and downstream regions, polar flybys that do not clearly sample either of the regions are not considered.

3. Results

We analyzed the RPWS electron density and LEMMS electron intensity data for the 12 selected flybys. Results show that RPWS data exhibit clear asymmetry between the upstream and downstream regions while LEMMS data do not. Table 2 summarizes the key data for each flyby.

3.1. Upstream–Downstream Asymmetry in RPWS Electron Density

Figure 3 shows RPWS electron density, n_e, as a function of radial distance between Cassini and Enceladus for the upstream and downstream flybys. The two panels reveal a clear upstream–downstream contrast in the near-Enceladus electron density profiles, with downstream flybys generally exhibiting prominent depletion signatures while upstream flybys do not. This difference is visualized in Figure 4, which shows the minimum Δn_e value (i.e., the largest depletion) upon approaching Enceladus for each flyby and further illustrates the stronger negative anomalies of the downstream encounters.

Depletions in electron density are observed for all downstream flybys around closest approach despite variations in the background density (see Figure 3). In particular, E3, E4, E5, E6, and E15 exhibit larger drops. Figure 4 and Table 2 show that electron density dropouts for downstream flybys range from -6.86 to -62.17 cm^{-3}. For the four close flybys with similar inclined trajectories (E3, E4, E5, E6) (see Figure 2), E3 and E5 recorded substantial negative anomalies of more than 55 cm^{-3}, whereas smaller depletions (-28.86 and -15.96 cm^{-3}) are observed during E4 and E6. All four flybys, however, reach similar minimum absolute electron densities between 15 and 25 cm^{-3} in the downstream region, indicating that the large contrast in Δn_e is primarily caused by variations in background electron density among flybys (see Figure 3).

In contrast, upstream flybys generally do not exhibit such obvious dropout patterns and only display fluctuations around the background density near closest approach (see Figure 3). Although E0, E1, and E16 show slight decreases near closest approach following a gradual increase in density as Cassini approached Enceladus, these depletion signatures are not clearly evident in the RPWS spectrograms. Moreover, the minima observed are comparable to the respective background densities. Figure 4 and Table 2 show that electron densities do not drop by more than 6 cm^{-3} below the background values during all upstream flybys.

Figure 5 maps the electron density anomaly on the x–y and x–z planes and reveals a clear spatial asymmetry. Data points in the upstream region ($x < 0$) near Enceladus remain close to or modestly above the ambient background level. In contrast, data points in or near the downstream geometric wake show substantial negative anomalies. Notably, in the E3 flyby, the pronounced depletion continued over the south pole.

Three flybys (E8, E15, E20) passed through the downstream region at larger distances from Enceladus and show differences in the extent of depletion. At closest approach, E15 was located farther downstream, at around 6 R_{Enc} in the x-direction and slightly below the geometric wake ($z \approx -1.4$ R_{Enc}). A significant depletion of -51.23 cm^{-3} is observed for E15. Intriguingly, this depletion occurs after, rather than at, closest approach, coinciding with the time when Cassini entered the wake shadow on the x–y plane. On the other hand, E8 and E20

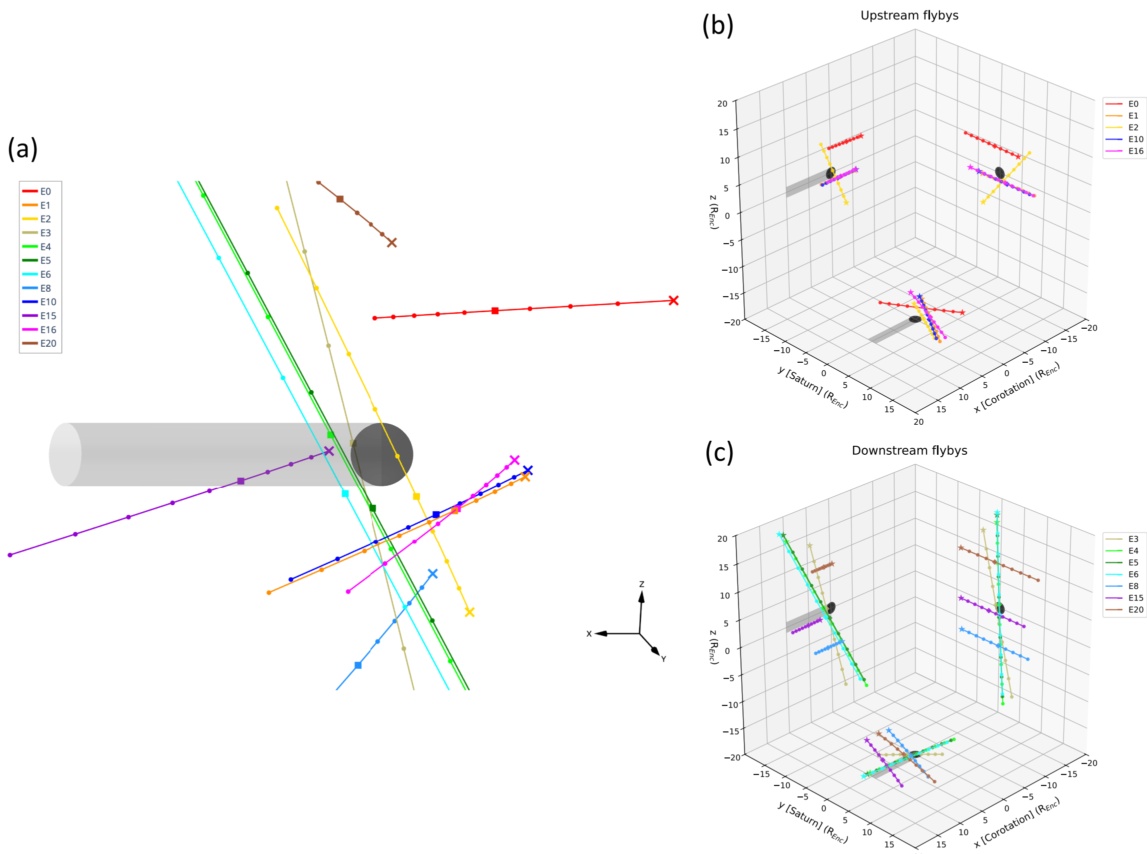

Figure 2. Overview of trajectories of Cassini flybys used in the study. (a) 3D close-up view of all trajectories. Squares and crosses indicate the closest approach and starting positions, respectively. The black sphere represents Enceladus and the gray cylinder represents the downstream geometric wake. (b), (c) Projections of trajectories (±5 minutes from closest approach) on x–y, x–z, and y–z planes for (b) upstream and (c) downstream flybys. Stars indicate the starting point, and diamonds mark the positions of closest approach.

Table 2
Summary of Key Data Values for Flybys Used in This Study

Flyby	Geometry	$n_{e,bg}$ (cm^{-3})	$n_{e,min}$ (cm^{-3})	$n_{e,min} - n_{e,bg}$ (cm^{-3})	I_{bg} (cm^{-2} sr^{-1} s^{-1} keV^{-1})	I_{min} (cm^{-2} sr^{-1} s^{-1} keV^{-1})	I_{min}/I_{bg} ($x10^{-3}$)
E0	Upstream, horizontal	129.23	130.30	1.07	29.39	0.7758	26.40
E1	Upstream, horizontal	62.07	60.18	−1.89	5.06	0.0889	17.58
E2	Upstream, inclined	76.17	70.74	−5.43	9.39	0.0269	2.87
E3	Downstream, inclined	81.33	19.16	−62.17	28.03	0.0000	0.00
E4	Downstream, inclined	44.45	15.59	−28.86	54.21	0.0065	0.12
E5	Downstream, inclined	81.86	25.15	−56.71	76.43	0.0027	0.04
E6	Downstream, inclined	40.44	24.48	−15.96	49.08	0.0108	0.22
E8	Downstream, horizontal, far south	45.23	33.25	−11.98	59.53	22.6183	379.96
E10	Upstream, horizontal	50.77	46.34	−4.43	29.18	0.0323	1.11
E15	Downstream (far), horizontal	92.60	41.37	−51.23	24.93	21.1472	848.19
E16	Upstream, horizontal	113.94	111.70	−2.24	44.32	0.2514	5.67
E20	Downstream, horizontal, far north	58.30	51.44	−6.86	4.59	0.0323	7.04

Note. $n_{e,bg}$ is the RPWS background electron density and $n_{e,min}$ is the minimum RPWS electron density observed upon approaching Enceladus. I_{bg} is the background electron intensity and I_{min} is the minimum electron intensity observed for the LEMMS E4 channel. All values shown in the table, except for I_{min}, are corrected to two decimal places. I_{min} values are corrected to four decimal places to better display the small values.

passed far south ($z \approx -7.27\ R_{Enc}$) and far north ($z \approx 8.13\ R_{Enc}$) of Enceladus, respectively. Despite the spacecraft being within 2 R_{Enc} in the x-direction during both encounters, only moderate depletions of −11.98 and −6.86 cm^{-3} are shown. These distant flybys may help constrain the spatial extent of the downstream interaction region.

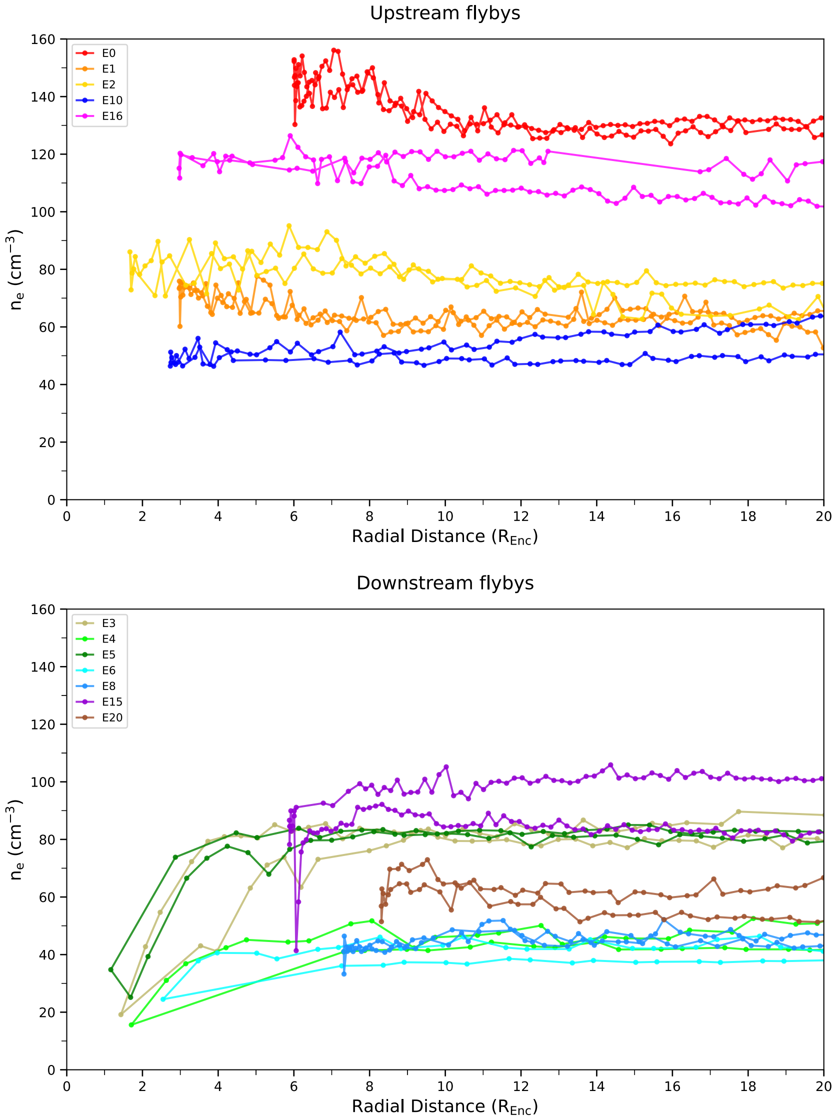

Figure 3. RPWS electron density versus radial distance between Cassini and Enceladus (in R_{Enc}) for upstream (upper panel) and downstream (lower panel) flybys.

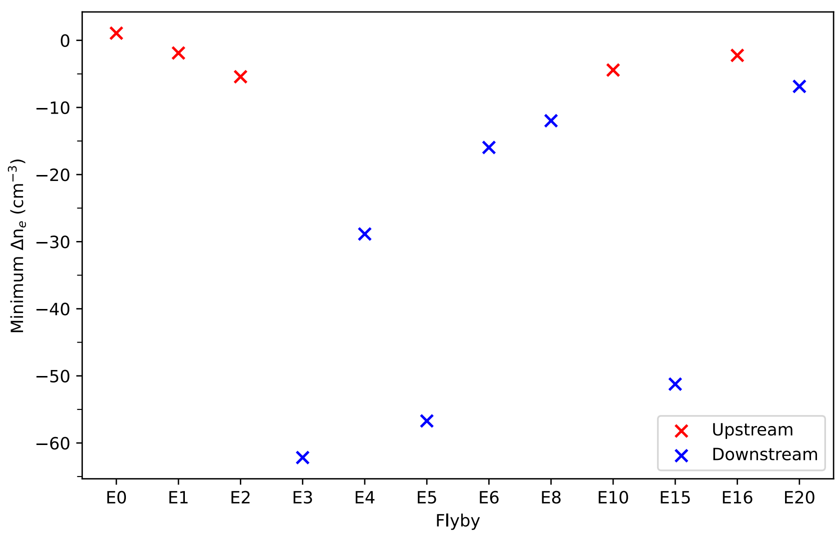

Figure 4. Minimum RPWS electron density anomaly Δn_e for all selected flybys. Red and blue crosses represent upstream and downstream flybys, respectively. A more negative value indicates stronger depletion.

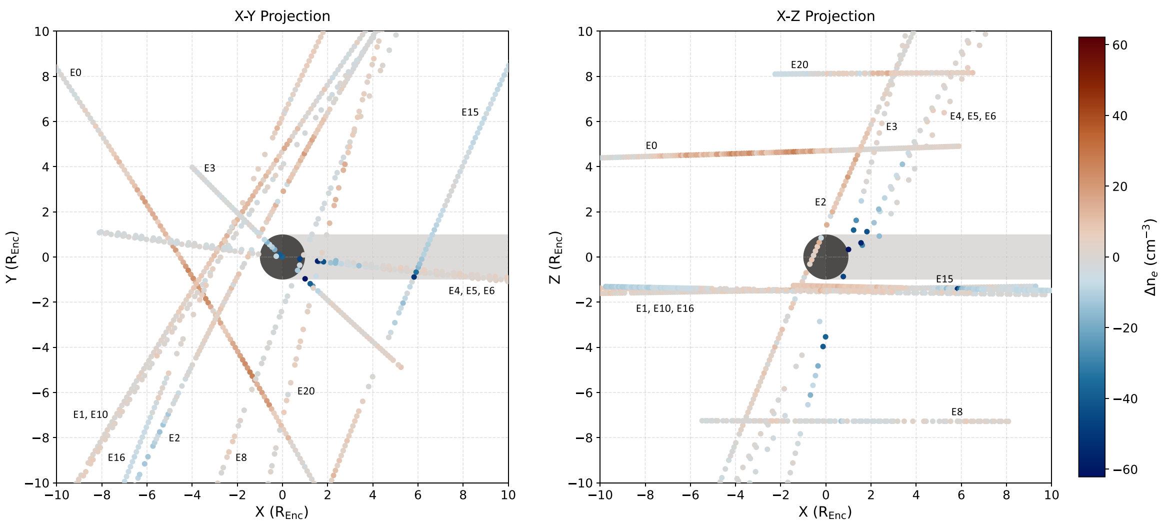

Figure 5. Projection of Cassini Enceladus flyby trajectories on the *x–y* (left) and *x–z* (right) planes. The colors of the markers indicate the RPWS electron density anomaly Δn_e. The black circle represents Enceladus, and the gray shaded rectangle represents the downstream geometric wake.

3.2. Comparison between RPWS and LEMMS Electron Data

The RPWS electron density largely represents cold electrons while LEMMS samples energetic electrons. Figure 6 compares the time series of RPWS electron density and LEMMS E4 electron intensity for upstream and downstream flybys, plotted as a function of time to closest approach in minutes. The RPWS density displays strong upstream–downstream asymmetry as described in Section 3.1, where upstream encounters show only modest deviations from the background level near closest approach, whereas downstream encounters commonly exhibit pronounced density depletions centered within 1 minute of closest approach. In contrast, the LEMMS E4 electron intensity often shows broad depletion features regardless of flyby geometry, though the dropouts are not always centered at closest approach. Figure 7 further illustrates the absence of upstream–downstream asymmetry in LEMMS data by showing the electron intensity ratio R_I ($R_I = I_{\min}/I_{bg}$, see Section 2.2) for all the selected flybys. Smaller ratios correspond to stronger depletions. The ratios span multiple orders of magnitude across the full set of flybys, with no obvious upstream–downstream variation. This contrasts with the RPWS electron density anomaly results (see Section 3.1), which show a clear distinction between upstream (weak depletion) and downstream (strong depletion) flybys in Figure 4.

For downstream flybys shown in Figure 6(b), most of them display concurrent depletions in RPWS electron density and LEMMS electron intensity. In particular, the substantial RPWS electron density dropouts of the low-altitude inclined passes (E3–E6) largely coincide with the strong LEMMS electron intensity depletions. These parallel signatures indicate that electrons over a wide energy range can be removed or are absent in the downstream interaction region. An exception is the E15 flyby. A large depletion of -51.23 cm^{-3} is observed in the RPWS data, but there is no observable intensity reduction signature in the LEMMS data.

For the upstream flybys in Figure 6(a), the RPWS electron densities remain close to the flyby-specific background values, and the negative anomalies are small (<5.43 cm^{-3}) (see Section 3.1). Nevertheless, all of them show clear LEMMS electron intensity decreases within a few minutes of closest approach. This contrast implies that the low- and high-energy electron populations may be governed by different physical processes in the vicinity of Enceladus.

4. Discussion and Summary

By analyzing the electron density distribution using RPWS data from Cassini's flybys of Enceladus, we reveal a systematic asymmetry between the upstream and downstream environments. For downstream events, the density depletion is significantly more pronounced, extending up to $\sim$8 $R_{\rm Enc}$ — well beyond the plasma wake region. Previous studies have also indicated that the electron density decrease is not due to typical plasma wake effects, but rather to dust absorption of electrons in a dust trail downstream of the moon, which extends a few Enceladus radii in the vertical (*z*-axis) direction (M. W. Morooka et al. 2011; I. A. D. Engelhardt et al. 2015). Notably, the upstream plasma flow relative to Enceladus is sub-Alfvénic; consequently, Alfvén wings would form in the downstream region, extending much farther in the north–south direction (S. Simon et al. 2011), thus offering a potential explanation for the downstream electron depletion.

The strongest depletions occur in the downstream wake and over the south pole, indicating that the density decrease is not only due to obstruction by the solid body of Enceladus. The occurrence of large negative density anomalies below the equatorial plane is consistent with the south-polar origin of the plume. The southern plume likely enhances the depletion by producing dust grains that subsequently absorb electrons, consistent with previous interpretations of electron loss near the Enceladus plume environment (W. M. Farrell et al. 2009; M. W. Morooka et al. 2011; T. W. Hill et al. 2012; I. A. D. Engelhardt et al. 2015).

In addition, the downstream distant flybys provide insight into the spatial extent of the interaction region. A significant depletion signature is observed 6 $R_{\rm Enc}$ downstream, and moderate dropouts are detected farther north ($\sim$8 $R_{\rm Enc}$) and south (~-7 $R_{\rm Enc}$). This suggests that the interaction region extends in both the downstream (positive *x*-axis) and vertical (*z*-axis) directions but is likely constrained along the *y*-axis, as implied by the E15 flyby.

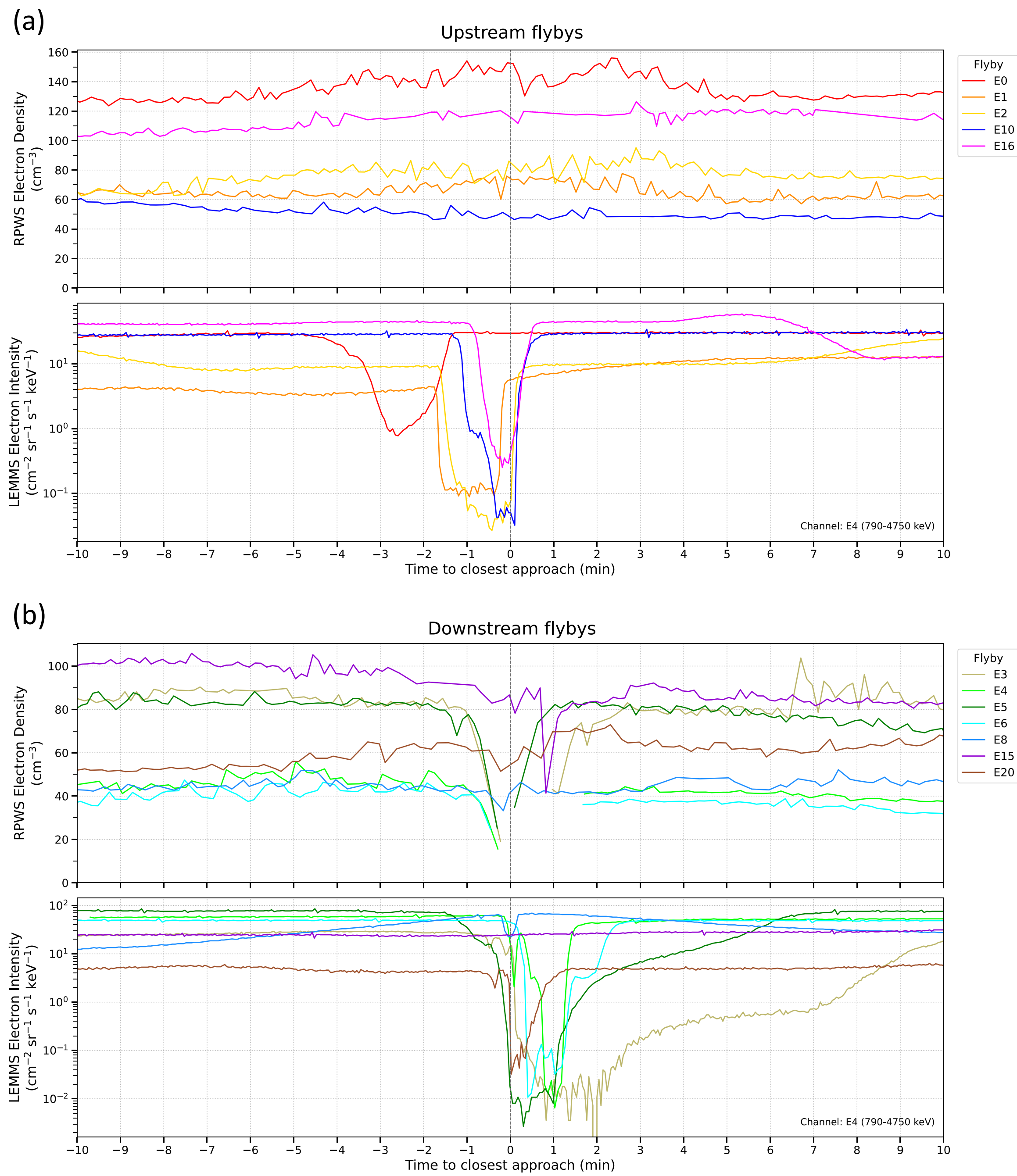

Figure 6. RPWS electron density and LEMMS E4 electron intensity for (a) upstream and (b) downstream Enceladus flybys, plotted as a function of time relative to closest approach (in minutes). The upper subplots show the RPWS data, and the lower subplots show the LEMMS data in logarithmic scale. The vertical dashed line marks the closest approach.

The clear differences between the RPWS and LEMMS datasets likely arise from two main factors: (1) RPWS data represent electron density, whereas LEMMS data include only energetic electrons. It is possible that cold electrons behave differently from energetic electrons. (2) The depletion of energetic electrons may be related to surface absorption, and thus depletions are observed not only during downstream flybys but also during upstream ones. In contrast, the electron depletions observed by RPWS may be linked to larger-scale processes, such as Alfvén wings, so that depletion occurs only in downstream flybys. Furthermore, although a single LEMMS measurement only corresponds to the energetic electron intensity at one specific pitch angle, dropouts are observed across a wide range of pitch angles ($\sim 11° - 152°$) across flybys. Therefore, it is unlikely that the pitch angle and difference in angular resolution between the two instruments caused the observed distinction. The discrepancies between the two datasets warrant further detailed analysis in the future, ideally in conjunction with numerical simulations.

In summary, we conducted a systematic survey of electron density variations near Enceladus using Cassini RPWS measurements from 12 targeted flybys, supplemented by LEMMS energetic electron observations. The main results are as follows.

First, RPWS electron density exhibits a clear upstream–downstream asymmetry. Downstream flybys show pronounced

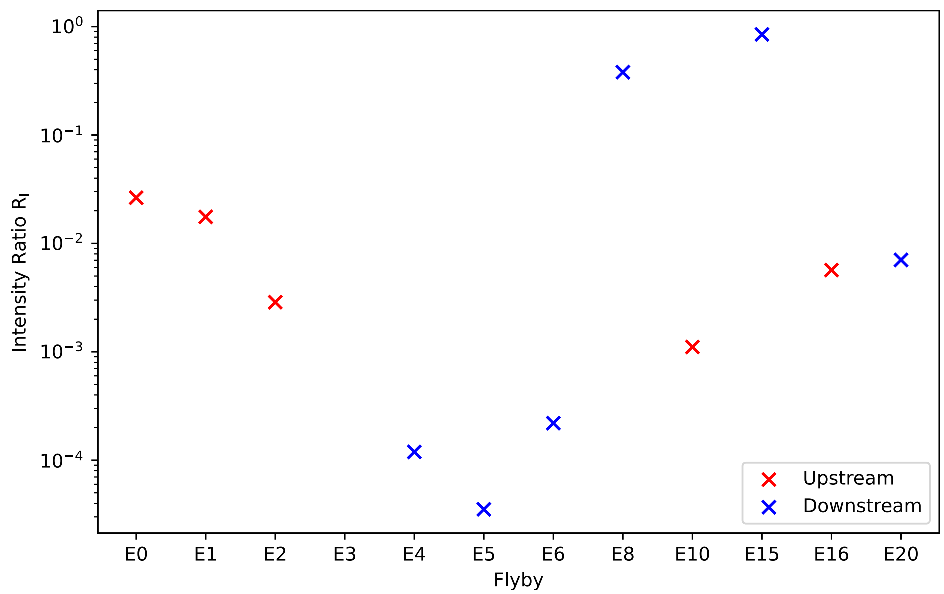

Figure 7. LEMMS electron intensity ratio (R_I) for all selected flybys, calculated by $I_{\min}/I_{\text{bg}}$ as described in Section 2.2. The *y*-axis is in logarithmic scale. Red and blue crosses represent upstream and downstream flybys, respectively. Smaller ratios indicate stronger depletions. No data are shown for the E3 flyby as the ratio is 0 and cannot be displayed on a logarithmic plot.

density depletions near Enceladus, with anomalies reaching up to ~60 cm^{-3} below background levels, whereas upstream flybys display only modest variations on the order of a few cm^{-3} and do not exhibit comparable depletion signatures. This is consistent with the presence of dust trail and Alfvén wing structures downstream of Enceladus.

Second, the magnitude of downstream density depletions depends on flyby geometry. Pronounced depletions are generally observed when traversing the downstream wake and near the southern plume region, while flybys that are located farther from the equatorial plane in the vertical direction show weaker perturbations. Moreover, during the E15 flyby, the largest depletion appears after the spacecraft enters the downstream geometric wake. These results highlight the role of the plume in driving electron depletion and help constrain the spatial scale of the interaction region.

Third, LEMMS energetic electron observations do not show the same upstream–downstream asymmetry as RPWS measurements, with intensity dropouts occurring in both regions and no systematic upstream–downstream dependence for the minimum-to-background intensity ratios. This is likely due to the different energy ranges of electrons sampled by the two instruments, thus reflecting the varying behavior of electrons with energy and the distinct physical processes governing cold and energetic electrons near Enceladus.

While further modeling is needed to elucidate the underlying physical processes, our results provide a comprehensive characterization of electron perturbations across space and energy based on observations.

Acknowledgments

We acknowledge usage of data from the Planetary Plasma Interaction Node (PPI) of the NASA Planetary Data System (PDS) archives, including Cassini RPWS Electron Densities from Upper Hybrid and Plasma Wave Frequencies (A. M. Persoon et al. 2019) and MIMI LEMMS Calibrated Bundle (J. Vandegriff 2024). Z.Y. acknowledges the General Program of the National Natural Science Foundation of China (grant 42374212), the Research Grants Council (RGC) General Research Fund (grant 17309124), and Project (JLFS/P-702/24) of Hong Kong RGC Co-funding Mechanism on Joint Laboratories with the Chinese Academy of Science. S.T. would like to acknowledge the National Key Research and Development Program of China (No. 2025YFF0811801). F.W.C.L. acknowledges the Summer Research Fellowship 2023–24 organized by the Faculty of Science, the University of Hong Kong, and help with LEMMS data processing from Tianshu Qin in the Department of Earth and Planetary Sciences, the University of Hong Kong.

ORCID iDs

Zhonghua Yao https://orcid.org/0000-0001-6826-2486
Shangchun Teng https://orcid.org/0000-0002-9480-8136

References

Dougherty, M. K., Khurana, K. K., Neubauer, F. M., et al. 2006, Sci, 311, 1406
Engelhardt, I. A. D., Wahlund, J. E., Andrews, D. J., et al. 2015, P&SS, 117, 453
Farrell, W. M., Kurth, W. S., Gurnett, D. A., et al. 2009, GeoRL, 36, L10203
Gurnett, D. A., & Bhattacharjee, A. 2005, Introduction to Plasma Physics: With Space and Laboratory Applications (Cambridge Univ. Press)
Gurnett, D. A., Kurth, W. S., Kirchner, D. L., et al. 2004, SSRv, 114, 395
Hansen, C. J., Esposito, L., Stewart, A. I. F., et al. 2006, Sci, 311, 1422
Hill, T. W., Thomsen, M. F., Tokar, R. L., et al. 2012, JGRA, 117, A05209
Krimigis, S. M., Mitchell, D. G., Hamilton, D. C., et al. 2004, SSRv, 114, 233
Krupp, N., Kotova, A., Roussos, E., et al. 2020, JGRA, 125, e2019JA027688
Krupp, N., Roussos, E., Kollmann, P., et al. 2012, Icar, 218, 433
Krupp, N., Roussos, E., Paranicas, C., et al. 2018, Icar, 306, 256
Kurth, W. S., Averkamp, T. F., Gurnett, D. A., & Wang, Z. 2006, P&SS, 54, 988
Morooka, M. W., Wahlund, J. E., Eriksson, A. I., et al. 2011, JGRA, 116, A12221
Paranicas, C., Roussos, E., Dialynas, K., et al. 2022, ApJ, 934, 11
Persoon, A. M., Groene, J. B., West, E. E., et al. 2019, Cassini RPWS Electron Densities from Upper Hybrid and Plasma Wave Frequencies, NASA Planetary Data System, doi:10.17189/1518302
Persoon, A. M., Kurth, W. S., Gurnett, D. A., et al. 2020, JGRA, 125, e2019JA027768
Pontius, D. H., Jr., & Hill, T. W. 2006, JGRA, 111, A09214

Porco, C. C., Helfenstein, P., Thomas, P. C., et al. 2006, Sci, 311, 1393
Simon, S., Saur, J., Kriegel, H., et al. 2011, JGRA, 116, A04221
Smith, H. T., Johnson, R. E., Perry, M. E., et al. 2010, JGRA, 115, A10252
Spahn, F., Schmidt, J., Albers, N., et al. 2006, Sci, 311, 1416
Tokar, R. L., Johnson, R. E., Hill, T. W., et al. 2006, Sci, 311, 1409
Vandegriff, J. 2024, Cassini MIMI LEMMS Calibrated Bundle, NASA Planetary Data System, doi:10.17189/r4v7-mv45
Vandergriff, J., DiFabio, R., Hamilton, D., et al. 2018, PDS3 Cassini/MIMI Instrument Data User Guide, NASA Planetary Data System, doi:10.17189/1522469
Waite, J. H., Combi, M. R., Ip, W.-H., et al. 2006, Sci, 311, 1419
Wang, Z., Gurnett, D. A., Averkamp, T. F., Persoon, A. M., & Kurth, W. S. 2006, P&SS, 54, 957
Ye, S. Y., Gurnett, D. A., Kurth, W. S., et al. 2014, JGRA, 119, 3373